International Journal of Innovative Research and Scientific Studies, 8(5) 2025, pages: 1255-1270

IJIRSS
International Journal of Innovative Research & Scientific Studies

ISSN: 2617-6548

URL: www.ijirss.com

Improving in microhardness of C45 steel obtained via electron beam hardening using a one-factor-at-a-time technique

Angel Anchev[1,4*], Borislav Stoyanov[2,4], Milka Atanasova[1,4], Yaroslav Argirov[3], Boris Petkov[1,4]

[1]*Department of Material Science and Mechanics of Materials, Technical University of Gabrovo, 5300 Gabrovo, Bulgaria.*
[2]*Department of Industrial Design and Textile Engineering, Technical University of Gabrovo, 5300 Gabrovo, Bulgaria.*
[3]*Department of Material Sciences, Technical University of Varna, 9010 Varna, Bulgaria.*
[4]*Center of competence "Smart mechatronic, eco-and energy-saving systems and technologies", Technical University of Gabrovo, 5300 Gabrovo, Bulgaria.*

Corresponding author: Angel Anchev (*Email: anchev@tugab.bg*)

Abstract

This article presents a novel electron beam hardening (EBH) process for C45 steel cylindrical specimens in an as-received state, utilizing continuous irradiation with power in the range of 720–2070 W and line scanning in the axial direction. The influence of operating parameters (i.e., electron beam current, workpiece velocity, scanning frequency, and focal length) on microhardness is examined using a one-factor-at-a-time technique. Scanning electron microscopy images reveal pronounced surface transformation hardening of C45 steel, resulting in martensite transformation and the formation of a pseudo-amorphous structure in the surface layer. The maximum surface microhardness obtained, HV_0.05=903, is three times greater than that achieved after turning (the step before EBH). The electron beam current and workpiece velocity significantly influence the thermal processes in the surface layers and, consequently, the microhardness. Based on the experimental results, the optimal ranges of the operating parameters have been defined.

Keywords: C45 carbon steel, Electron beam hardening, Microhardness, Microstructure modification, One factor-at-a-time technique.

DOI: 10.53894/ijirss.v8i5.9089
Funding: This work is supported by the Bulgarian Ministry of Education and Science and the Technical University of Gabrovo, Bulgaria (Grant number: NIP2025-5), and by the European Regional Development Fund within the Operational Programme "Research, Innovation and Digitalization for Intelligent Transformation 2021–2027", Bulgaria (Grant number: BG16RFPR002-1.014-0005).
History: Received: 13 June 2025 / **Revised:** 21 July 2025 / **Accepted:** 23 July 2025 / **Published:** 5 August 2025

Competing Interests: The authors declare that they have no competing interests.
Authors' Contributions: Conceptualization, Writing–Original Draft Preparation, Resources, Investigation, Supervision, Project Administration, Funding Acquisition, Angel Anchev (A.A.); Conceptualization, Writing–Original Draft Preparation, Resources, Investigation, Visualization, Funding Acquisition, Borislav Stoyanov (B.S.); Methodology, Software, Validation, Writing–Review and Editing, Project Administration, Milka Atanasova (M.A.); Methodology, Formal Analysis, Investigation, Yaroslav Argirov (Y.A.); Software, Formal Analysis, Data Curation, Visualization, Boris Petkov (B.P.). All authors have read and agreed to the published version of the manuscript.
Transparency: The authors confirm that the manuscript is an honest, accurate, and transparent account of the study; that no vital features of the study have been omitted; and that any discrepancies from the study as planned have been explained. This study followed all ethical practices during writing.
Publisher: Innovative Research Publishing

1. Introduction

C45 (AISI 1045) medium-carbon steel offers a balanced combination of high tensile strength, good machinability, hardness, wear resistance, weldability, and cost-effectiveness. Its versatility makes it suitable for various industries, including automotive, construction, heavy machinery, and mechanical parts manufacturing. The steel's high tensile and fatigue strengths are advantageous for gears, shafts, axles, bolts, and other components subjected to high loads.

The operation of the machine and structural elements leads to inevitable damage caused by wear, fatigue, and corrosion. This degradation process develops over time, mainly in the surface layers (SLs) of the metal components, for the following reasons: 1) transmission of power flow between the contacting parts; 2) the operating stresses are maximum in SLs; and 3) SLs are subjected to direct impact with the environment, which is often aggressive. Therefore, the life cycle and operating conditions of the components depend on the complex combination of topographical, physical-mechanical, chemical, and metallurgical characteristics of the SL, known as surface integrity (SI) [1]. The final SI is determined by the SL's evolution during the entire cycle of manufacturing, but the finishing process is of decisive importance. Ultimately, increasing the strength of metal components by modifying only their SLs is particularly effective.

There are two main approaches for surface hardening: 1) strain hardening based on surface cold working, and 2) transformation surface hardening. Both approaches have been applied to a wide range of steels: medium-carbon steels, alloy structural steels, stainless steels, and tool steels.

Surface cold working processes are considered dynamic (shot peening [2], laser shock peening [3], cavitation peening [4] or static (burnishing). The burnishing processes are more suitable for machining rotational parts. According to the tangential contact between the deforming element (ball or roller) and the surface being treated, burnishing processes rely on rolling friction contact [5, 6] or sliding friction contact [7-9].

Transformation surface hardening processes are thermal processes resulting in phase and structural transformations during heating and cooling. Considering the possibility of changing the chemical composition in the SLs, there are two types of transformation surface hardening processes: 1) thermo-chemical diffusion processes, and 2) hardening without changing the chemical composition. Conventional variants of the first type include nitriding, carburizing, carbonitriding, and nitrocarburizing, which are widely employed to increase the hardness, wear resistance, and strength of structural and tool steels. A conventional example of the second type is induction hardening, which typically requires significant time and energy [10]. Laser beam and electron beam techniques use precisely focused energy with high intensity, providing very high heating and cooling rates without the need for external cooling. Applying intense and rapid thermal cycles to the SLs leads to ultrafast heating, melting, evaporation, and subsequent solidification [11, 12]. The microstructural changes and phase transformations, as well as the induced stresses, effectively increase the microhardness, wear resistance, and fatigue strength of the SLs. In addition, the desired bulk properties, such as toughness and ductility, are preserved, which is especially important for rotating steel components such as shafts and axles. Laser beam and electron beam techniques also provide precise control, making it possible to treat specific details or regions of the part. Moreover, these technologies enable high reproducibility, significantly shorter process duration than conventional heat treatment, very small deformations due to localized thermal impact, and low environmental impact.

The combination of different operating parameters (i.e., beam power, heating and cooling rates, beam scanning velocity, scan trajectory, and deflection mode) determines the performance and efficiency of the laser beam and electron beam techniques. In this way, different thermal effects in the SLs can be achieved, and thus different SIs. The transition to a liquid state of SLs is the physical basis of various surface modification processes, such as surface alloying [13, 14] and coating deposition [15-18] which are generally accompanied by a change in the chemical composition; however, surface modification processes without changes in the chemical composition have also been applied to a wide range of steels: low- and medium-carbon [19-21] low-alloy steel [22, 23] austenitic stainless steels [24-26] martensitic stainless steel [27] and tool steels [28, 29].

When the surface temperature is lower than the melting point of the material, the treated area remains in a solid state, but some structural and phase transformations occur. Essentially, this type of treatment leads to martensitic transformation and is mainly used for the surface hardening of steels. Owing to the higher cooling rate of processing, reaching values of 109 K/s in pulsed radiation mode, and 104-105 K/s in continuous radiation mode [12] metastable structures are formed, as well as a finer microstructure, leading to increased hardness and wear resistance of the SLs. Therefore, electron beam hardening (EBH) and laser beam hardening (LBH) are particularly effective for processing hypoeutectoid carbon steels and low-alloy structural steels. The effects of LBH on the strengthening and modification of SLs have been established for AISI 1040 [30, 31] and C45 (AISI 1045) [32-34] medium-carbon steels; and AISI 4340 [23] 25XM [35] and 50CrMo4 [36] alloy steels.

EBH enables more precise control, lower energy reflection factors, and more reproducible operational parameters than LBH [12], providing greater ability to control the structure and properties of the treated materials. Matlák et al. [22] investigated the influence of deflection modes (one-point, 6-point, 11-point, line, field, and meander), scanning velocity, and defocusing of the electron beam on the microstructure and hardened layer thickness in 42CrMo4 (AISI 4140) low-alloy steel plate specimens. They found that EBH induces a very fine martensitic microstructure with a hardness of over 700, and the maximum hardened depth was 1.49 mm. Choo et al. [37] studied the effects of beam power (in the range of 5.2–7.7 kW) in high-energy accelerated electron beam irradiation on the surface hardening and rotating bending fatigue behavior of AISI 4140 low-alloy steel specimens. Using this technique, a maximum hardness of 830 VHN was achieved, which was 2.5 times greater than the original material hardness, and an improvement in fatigue properties of approximately 35% was observed. The effects of continuous EBH on the surface hardening and microstructure modifications of high-strength low-alloy steel 30CrMnSiA, typically used in aerospace industries, were experimentally investigated by Fu et al. [38]. They reported that the microhardness value increased from 208 $HV_{0.2}$ in the base metal to 520 $HV_{0.2}$ in the irradiated area, while the surface roughness was relatively unchanged.

The studies devoted to EBH of AISI 1045 steel are sparse and mainly focused on plate specimens [20, 39]. According to the numerical model developed in Fu et al. [38], the efficiency of EBH in medium-carbon steel increases with the translational speed of the samples treated, and the power of the electron beam weakly influences the efficiency. Furthermore, the formation of the surface microstructure in AISI 1045 steel plate specimens by pseudospark-based pulsed EBH was investigated [39]. The superfast heating and cooling processes of the pseudospark-based pulsed electron beams are capable of promoting grain refinement and metastable structure formation in the SLs of AISI 1045 steel.

Notably, most studies are devoted to the modification of plate specimens using LBH and EBH, and few studies focus on rotational specimens [37]. Considering the wide application of C45 steel as a structural material for components obtained by rotational processing, it is necessary to develop an effective EBH process adapted for cylindrical C45 steel specimens. Rotational C45 steel specimens have been produced under LBH processing, in which the laser beam traverses the cylindrical surface in a helical line [32], but this scanning mode leads to significant inhomogeneity of the surface layer in the axial direction.

The primary aim of this study is to evaluate the influence of EBH operating parameters on the microhardness of C45 steel cylindrical specimens, utilizing continuous irradiation and line scanning in the axial direction. To examine the individual effects of different parameters (governing factors), a one-factor-at-a-time technique was employed. The process's effectiveness was assessed based on the following SI characteristics: surface microhardness, microhardness depth profile, and SL microstructure.

2. Materials and Methods

2.1. Material

Hot-rolled C45 steel bars (36 mm diameter) were used in an as-received state. The chemical composition was measured via optical emission spectrometry, with a resolution of 0.001 wt%. The mechanical characteristics were determined as the arithmetic means of the results obtained from three tensile tests at room temperature. A Zwick/Roell Vibrophore 100 testing machine (Ulm, Germany) was used for tensile tests. The working sections of the tensile test specimens had a diameter of 6 mm and a length of 30 mm. To determine the phase analysis, a Bruker D8 Advance diffractometer with specialized software (DIFFRAC.EVA V5.2, Billerica, MA, USA) was used [40].

2.2. Turning and Electron Beam Hardening

Turning was conducted using an Index Traub CNC lathe (Esslingen am Neckar, Germany) with a CNMG120404MQ cutting insert. The following turning parameters were established: velocity of, feed rate of, and cutting depth of. The specimen geometry after turning is shown in Figure 1. The roughness of the cylindrical surfaces after turning was in the range of $R_{a,init} = 1.03–1.673$ μm.

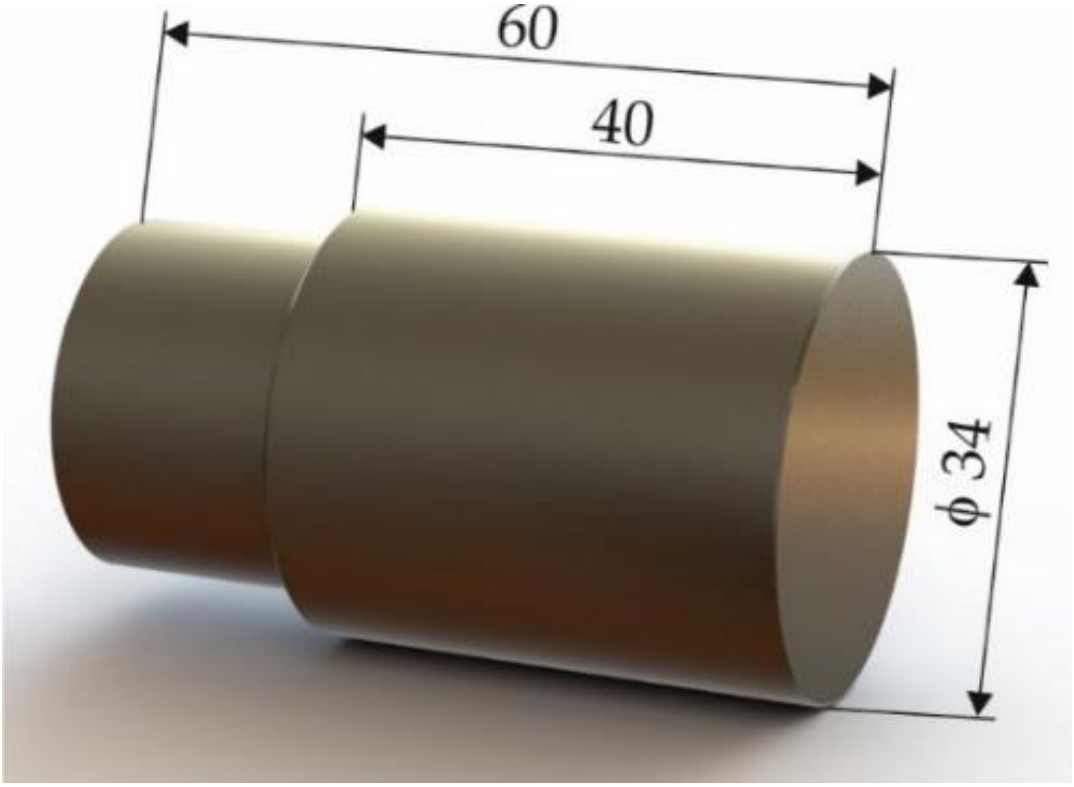

Figure 1.
Specimen geometry.

The EBH process was performed using an Evobeam μEBW Cube 400 machine (Evobeam GmbH, Germany). A schematic diagram of the novel EBH process, visualizing the operating parameters (governing factors), is shown in Figure 2a. To provide suitable conditions for conductive heat transfer, the treated area was symmetrically located on the specimen's cylindrical surface. A side view of the setup is shown in Figure 2b.
The irradiation power was controlled by regulating the electron beam current I_b, mA:

$$P = U.I_e\,, \qquad (1)$$

where the voltage is constant: U=60 kV. Thus, for a maximum electron beam current $I_{b,max} = 0.1$ A, the maximum irradiation power is $P_{max} = 6000$ W. The electron beam diameter (focal spot) is d=50 μm.

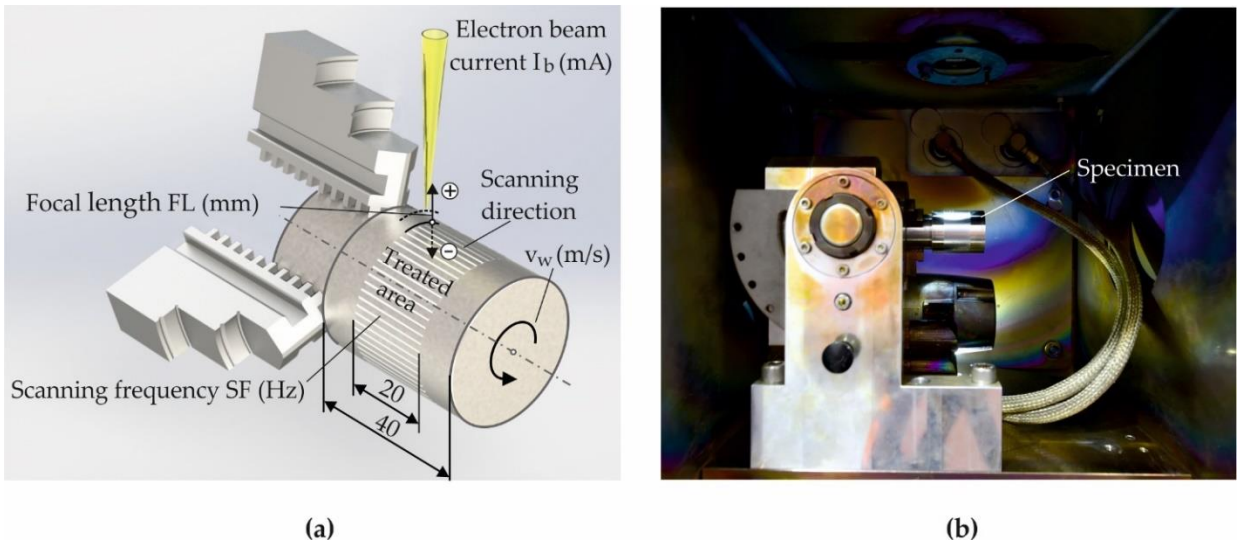

Figure 2.
EBH process: (a) principal scheme; (b) general view of equipment used.

The power density (PD) defined as the ratio of the irradiation power to the electron beam area A:

$$PD = \frac{P}{A} = \frac{U.I_e}{A}\,, \qquad (2)$$

For a focal length equal to zero, the area of the electron beam is approximately: $A = \frac{\pi d^2}{4} = 1.96349541 \times 10^{-9}$ mm^2.

The experimental study of the EBH process was conducted using a one-factor-at-a-time technique. The magnitudes of the governing factors were varied according to Table 1. Considering the investigated range of the electron beam current, the irradiation power varied in the range of $P = 720–2070$ W.

Table 1.
Magnitudes of the governing factor used during the experiments.

Governing factor	Magnitude					
Electron beam current I_b, mA	12	16.5	21	25.5	30	34.5
Workpiece velocity v_w, m/s	0.018	0.022	0.027	0.031	0.036	0.053
Scanning frequency SF, Hz	400	5300	10,200	15,100	20,000	-
Focal length FL, mm	+20	+15	+10	0	−5	−10

2.3. SI characteristics

A Zwick/Roell microhardness tester (Ulm, Germany) was used to measure the surface microhardness (0.05 kgf loading, 10 s holding time). The final surface microhardness value was recorded as the median of fifteen measurements performed on three equally spaced specimen generatrixes. R_a roughness parameters were measured using a Mitutoyo Surftest SJ-210 surface roughness tester (Kawasaki, Japan). The average arithmetic values were obtained from measurements performed on six equally spaced specimen generatrices. The microstructures were observed by scanning electron microscopy (SEM) using a Zeiss Evo 10 microscope (Jena, Germany).

3. Results

3.1. Material Identification

The chemical composition of the as-received steel samples is shown in Table 2.

Table 2.
Chemical composition of the as-received C45 steel in wt%.

C	Si	Mn	P	S	Cu	Al	Cr	Mo
0.457	0.295	0.568	<0.001	<0.001	0.052	<0.001	0.044	<0.001
Ni	**V**	**Ti**	**Nb**	**Co**	**W**	**Pb**	**Sn**	
0.011	0.046	0.009	0.003	<0.001	<0.001	<0.001	0.012	

Figure 3 shows the “stress-strain” curves obtained from tensile tests. The mechanical properties of the tensile-tested C45 steel were determined as arithmetic mean values Table 3.

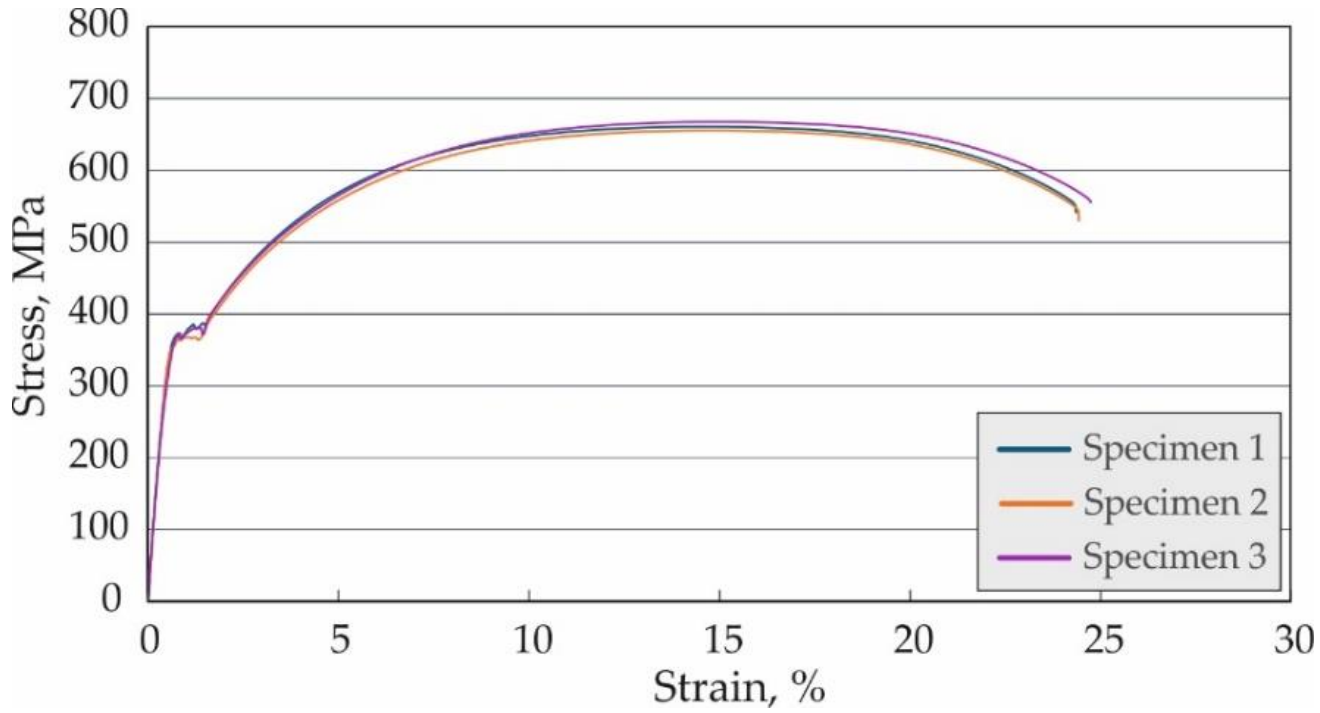

Figure 3.
Stress-strain curves of the as-received C45 steel.

Table 3.
Mechanical properties of the tensile-tested C45 steel.

Yield limit, MPa	Tensile strength, MPa	Elongation, %
357^{+7}_{-5}	666^{+1}_{-9}	$23.8^{+0.2}_{-0.1}$

The phase composition of the as-received steel is shown in Figure 4. The diffractogram shows a distribution of α-Fe peaks that are characteristic of hypoeutectoid steels, which have a base structure composed of ferrite and pearlite.

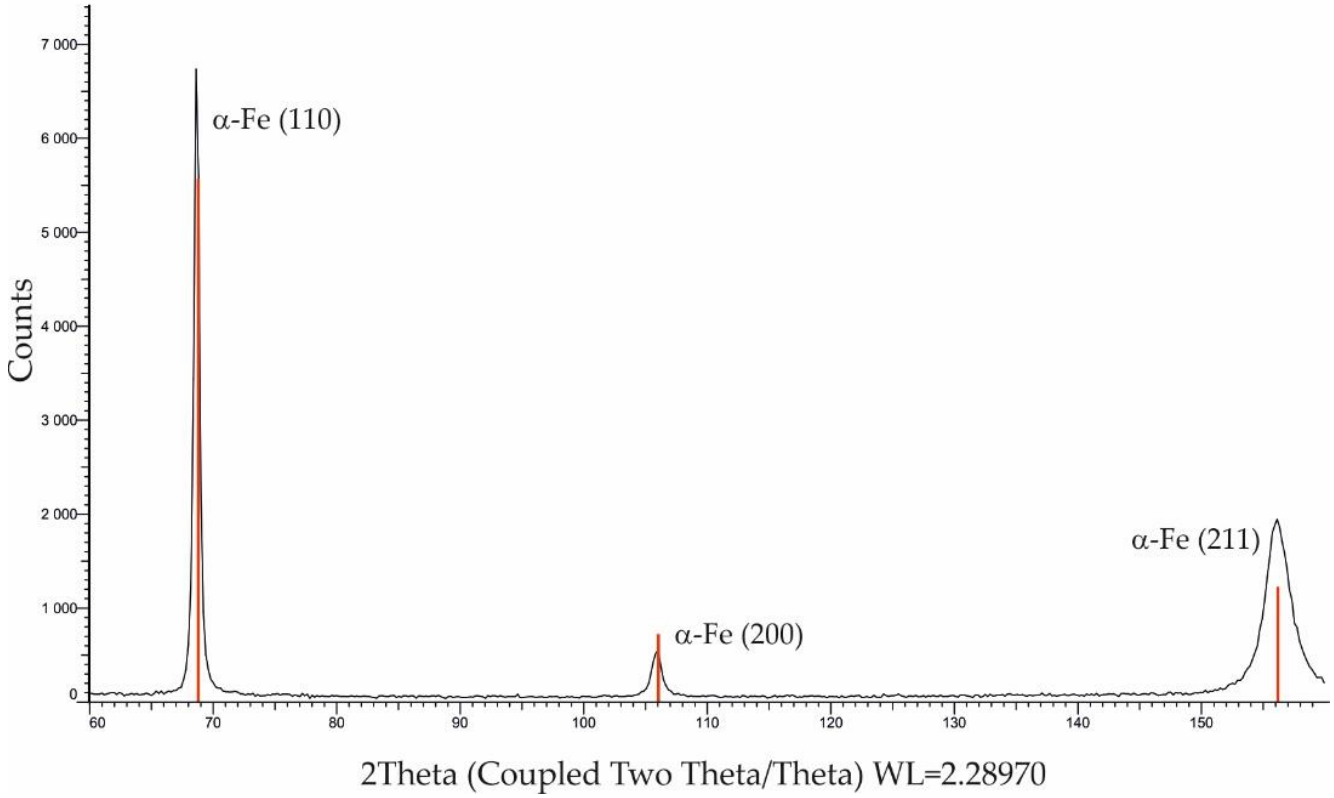

Figure 4.
Phase analysis of the as-received C45 steel.

3.2. Surface microhardness

3.2.1. Effect of I_b

Figure 5 shows the effect of the electron beam current I_b on surface microhardness, when the remaining three factors are maintained at constant intermediate values in the studied range (see Table 1).

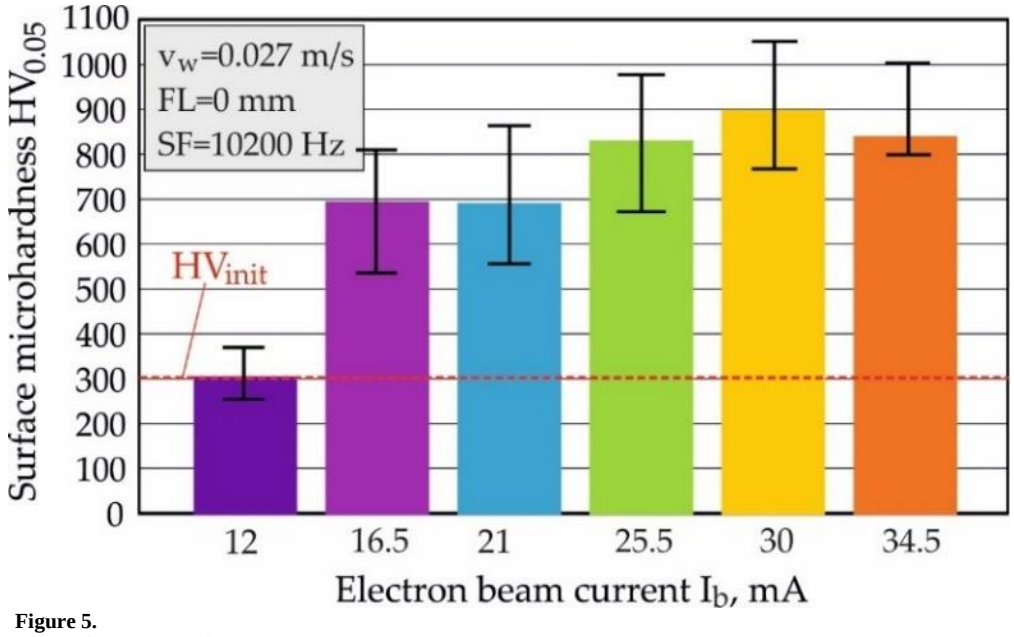

Figure 5.
Effect of I_b on the surface microhardness.

All studied values of the electron beam current significantly increase the surface microhardness, except for the smallest studied value of $I_b = 12$ mA. In this case, the electron beam power is too low, and the heat generated in the SLs is insufficient to generate significant microstructural changes. The surface microhardness increases with increasing I_b and reaches a maximum median value of $HV_{0.05} = 903$ at $I_b = 30$ mA. This microhardness value is three times greater than the initial microhardness after turning, $HV_{init} = 300$ (Figure 5). Further increasing the electron beam current does not appear to increase the microhardness, which appears to saturate and potentially decrease. Given that the workpiece velocity is unchanged, a likely reason for this is the insufficient cooling rate. The measured microhardness values showed some scattering (i.e., the width of the error bars) in the axial direction, but no periodic behavior was observed, typical of processes characterized by an overlapping effect in the axial direction [32].
The average roughness of the treated surfaces varied in the range of $–R_a = 0.258–1.071$ μm, With the lowest roughness corresponding to the highest beam current $I_b = 34.5$ mA. This is an indicator of surface melting phenomena [30].

3.2.2. Effect of v_w

The effect of workpiece velocity v_w on the surface, microhardness is shown in Figure 6. When other factors remain constant, the workpiece velocity determines the duration of the EBH process, and therefore, the amount of heat input. The surface microhardness initially increases and then saturates with the increase in workpiece velocity, in the range of $v_w = 0.018–0.036$ m/s. When the workpiece velocity was further increased to 0.053 m/s, which corresponds to a process duration of approximately 2 s, $HV_{0.05}$ drastically decreases because the heating is insufficient. Conversely, there is a tendency for a greater scattering of the measured surface microhardness values with the increasing workpiece velocity. The variation in $HV_{0.05}$ is maximum for $v_w = 0.053$ m/s, resulting in a range of 357.

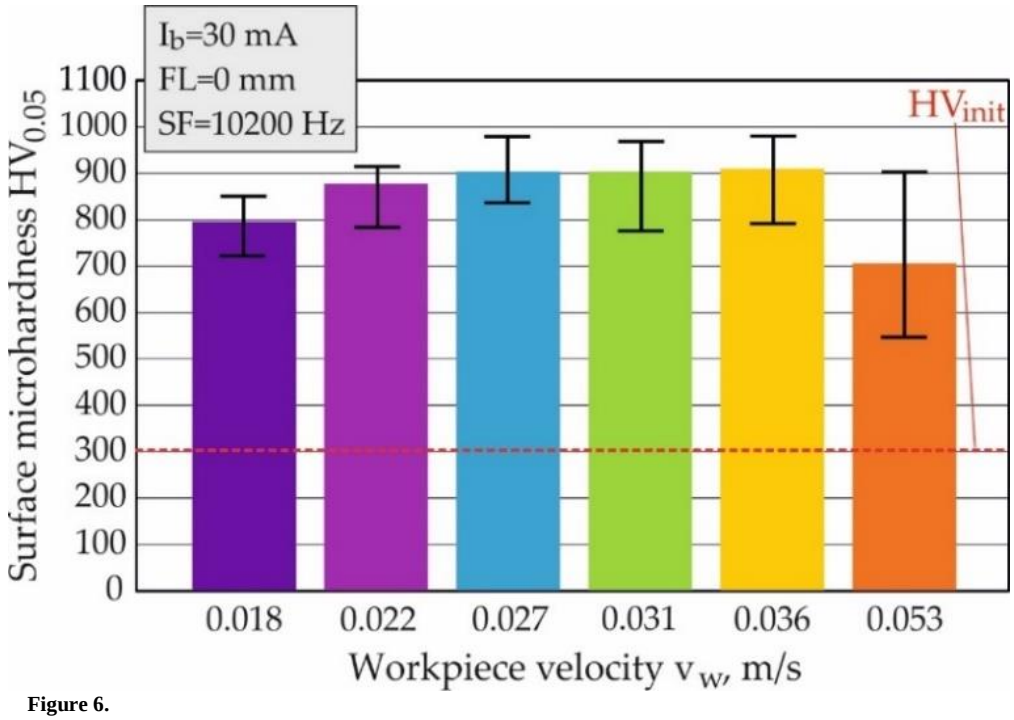

Figure 6.
Effect of v_w on the surface microhardness.

The average roughness of the specimens varies in a relatively wide range: $R_a = 0.192–1.294$ μm. The largest reduction in the initial roughness was obtained for the specimen processed with the lowest velocity ($v_w = 0.018$ m/s).

3.2.3. Effect of SF

The change in the scanning frequency (SF) has a relatively weak influence on the surface microhardness when the remaining three factors are maintained at constant values. Increasing the scanning frequency in the range of SF = 400–10,200 Hz leads to an increase in the surface microhardness, reaching a maximum median value of $HV_{0.05} = 882$ Figure 7. In contrast, the range of SF = 15,100–20,000 Hz leads to a slight decrease in $HV_{0.05}$, Despite the more uniform heating of the treated surface, the lowest scanning frequency (SF = 400 Hz) causes uneven heating due to the large step between the scanning lines in the circumferential direction. As a result, the treated surface exhibits a very rough topography and the greatest $HV_{0.05}$ scattering.

The average roughness of the treated surfaces varies in the range of: $R_a = 0.295–5.735$ μm. The roughness was reduced for all studied values of the scanning frequency, except for SF = 400 Hz, where marked deterioration was observed ($R_a = 5.735$ μm).

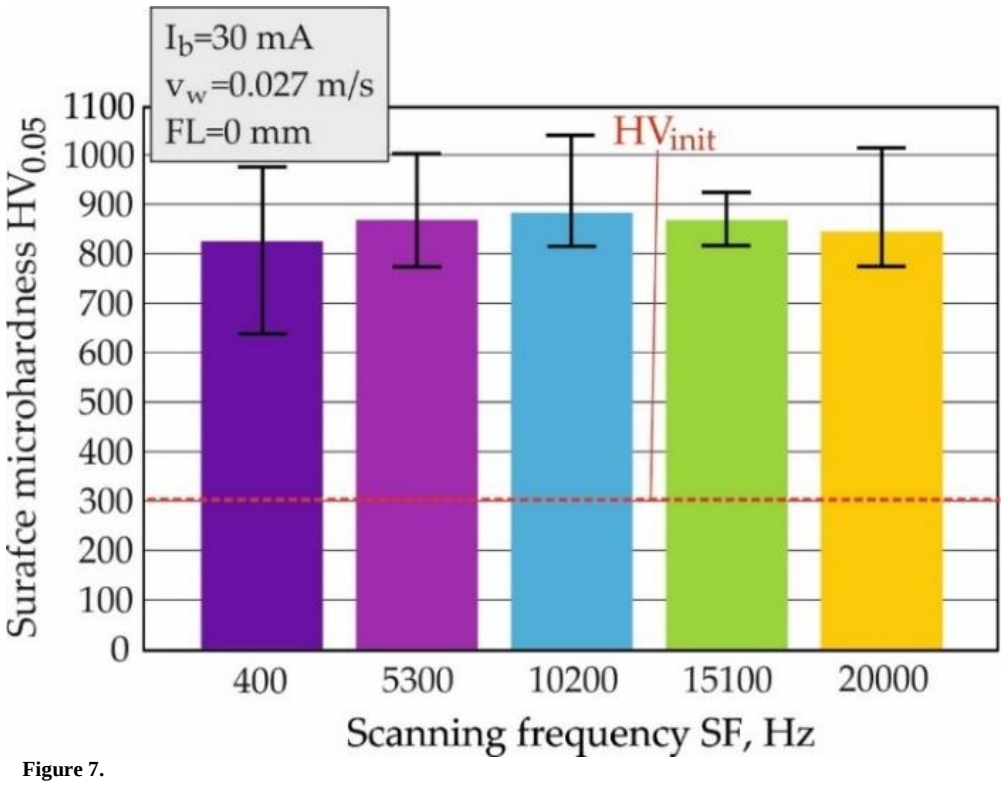

Figure 7.
Effect of SF on the surface microhardness.

3.2.4. Effect of FL

Figure 8 shows the influence of the focal length (FL) on the surface microhardness when the other parameters remain constant. With a decrease in the positive focal length in the range of FL = 5–20 mm, the surface microhardness $HV_{0.05}$ increases by 85. Notably, using the opposite FL values (FL = ±5 mm or FL = ±10 mm) leads to almost the same surface microhardness. Furthermore, the scatter of the measured surface microhardness decreases with a decrease in the absolute value of FL (i.e., the scatter is smallest for FL = 0 mm) (Figure 8).

The change in FL has little effect on the resulting average roughness, which varies in the range: R_a = 0.418–0.798 μm.

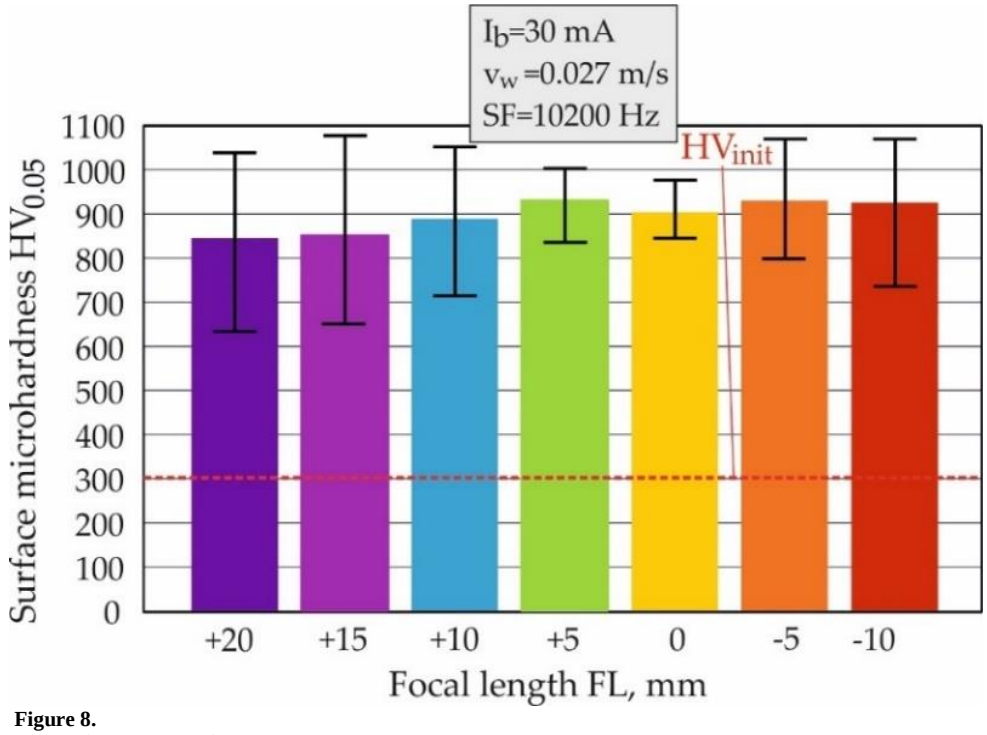

Figure 8.
Effect of FL on the surface microhardness.

3.2.5. Verification of the Repeatability

To assess the capabilities of the studied EBH process in reproducing surface microhardness values corresponding to specific technological parameters, the repeatability was evaluated. Four samples were subjected to EBH using the same parameters (Figure 9). The experimental results were practically identical in terms of the median $HV_{0.05}$ values.

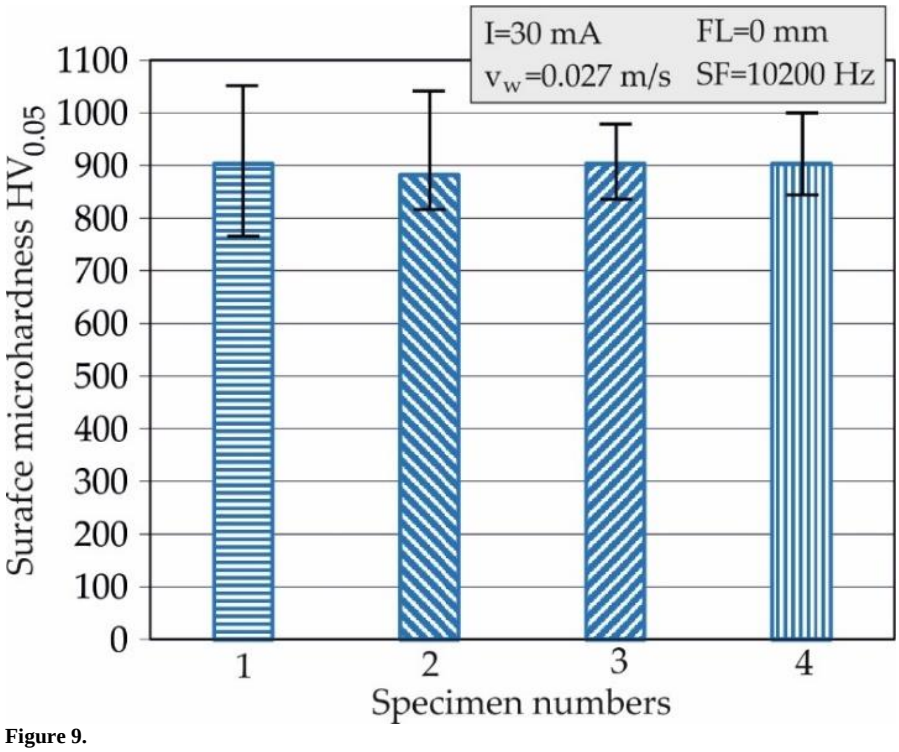

Figure 9.
Repeatability of the experimental results.

4. Discussion

The studied EBH process is a surface thermal process, and the efficiency depends on the amount of heat introduced to an area of the treated surface per unit time. A quantitative index of the thermal process is the power density PD, which correlates with the heat flux density obtained in the processing zone as a result of the conversion of the kinetic energy of electrons into heat. At constant voltage, the PD power density depends on the electron beam current I_b and the electron beam area A. When the remaining operating parameters are fixed, the generated inhomogeneous and non-stationary temperature field in the SL and the associated thermal processes depend on the irradiation time, which is directly proportional to the workpiece velocity v_w. Therefore, I_b and v_w significantly influence the amount of heat input and the balance between heating and cooling rates, and consequently, the structure and phase transformations in the SLs. The experimental results shown in Figs. 5 and 6 confirm that the changes in I_b and v_w in the studied ranges, lead to a significant change in the median surface microhardness. No hardening effect was observed when the EBH process was implemented using the electron beam current of $I_b = 12$ mA, and therefore, this value can be excluded from future studies.

At constant values of I_b, v_w, and FL, increasing the line scan frequency SF results in a greater number of electron beam line scans over an area of the treated surface per second. Therefore, using a larger value of the SF parameter causes two thermal effects: 1) more heat is generated for the same time (i.e., the power density increases), and 2) the step between the scan lines in the circular direction decreases, or the overlapping effect is reduced, which leads to more uniform heating of the treated surface. The first effect has a greater impact on thermal processes and on the resulting surface microhardness (see Figure 7), and the second effect has a dominant impact on reducing the height of the surface topography, which correlates with improved surface homogeneity. Considering the Gaussian distribution of the beam power density in the radial direction, a high scanning frequency helps minimize the beam inhomogeneity. Moreover, according to Fu et al. [38], continuous irradiation and a high scanning frequency during EBH may eliminate the beam inhomogeneity. In the present study, using $SF = 400$ Hz resulted in the lowest $HV_{0.05}$ value, the largest scatter of the measured values (Figure 7), significantly deteriorated roughness ($R_a = 5.74$ μm) and a pronounced overlapping effect in the circumferential direction. Therefore, the scanning frequency of $SF = 400$ Hz is inappropriate for the EBH of C45 steel cylindrical specimens.

Figure 10 shows the change in the electron beam spot size (i.e., the area of the beam irradiating the surface) for three FL values: $-a, 0, +a$. Owing to the physical nature of the irradiation, the electron beam area interacting with the surface is the same for opposite values of the focal length ($FL = \pm a$). However, when the focal spot is below the surface ($FL = -a$), a localized zone of relatively higher temperature is created at a certain depth. As a result, the generated temperature field partially differs from the temperature field corresponding to $FL = +a$. In all cases, the velocity of electrons decreases as they interact with the atoms in the metal at a given depth, mainly through elastic and inelastic collisions.

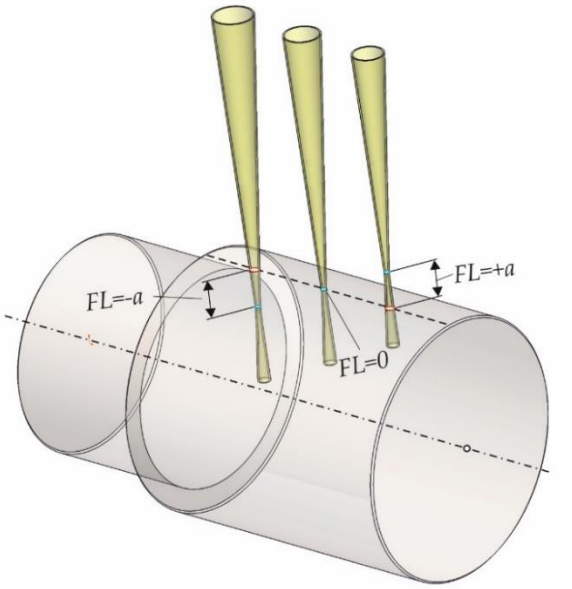

Figure 10.
Change in the electron beam area depending on the FL.

The extinction of the kinetic energy of the electron beam is greatest on the surface itself because the velocity of the electrons is highest. This explains the significant gradient of the generated heat as a function of depth from the surface, and the similar $HV_{0.05}$ results for opposite values of FL (see Figure 8). From this point of view, and accounting for the influence of FL on $HV_{0.05}$ scattering, it is not appropriate to use the FL values of ± 20 and ± 15 mm.

Considering that the thermal effects are mainly the result of conductive heat transfer, EBH with the same parameters and the same material dimensions leads to the same heat flux density, duration, and heating and cooling rates. Therefore, the amount of heat released per surface area is a function of the specific combination of operating parameters and can be controlled. Nonetheless, the reproducibility still depends on the structural inhomogeneity of the processed material.

The rapid change in concentrated thermal power causes a large temperature gradient in the SLs; therefore, the conditions for phase, structural, and aggregate changes are complex and difficult to control. To assess the influence of the electron beam current I_b on the microstructural modification, SEM images were taken at different magnifications for three specimens subjected to EBH with the same operating parameters ($v_w = 0.027$ m/s, SF = 10,200 Hz, FL = 0 mm), except for the electron beam current: $I_b = 16.5, 30$, and 34.5 mA.

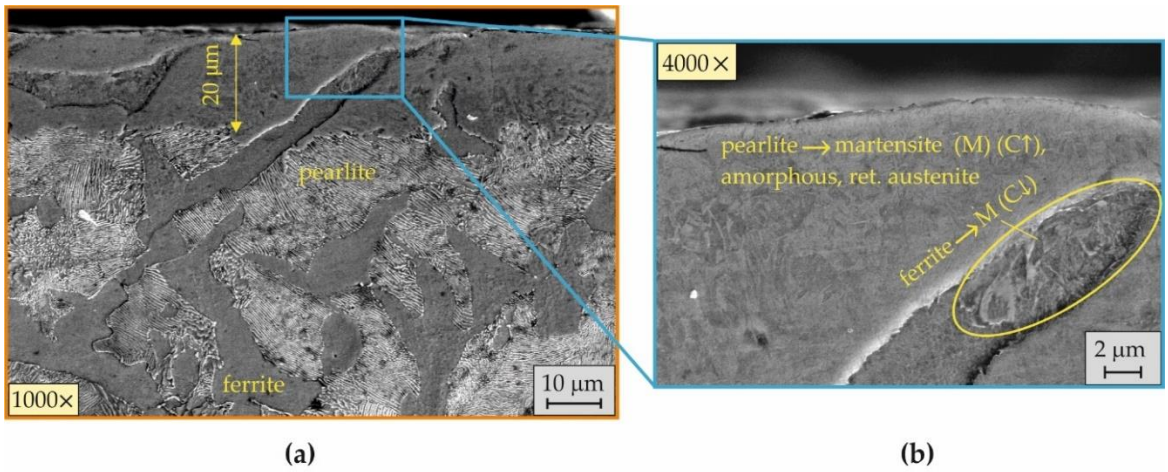

Figure 11.
Microstructure of the SLs after EBH with $I_b = 16.5$ mA.

Structural and phase changes in the specimen treated with $I_b = 16.5$mA are observed at a depth of approximately 20 µm in Figure 11a. The short time and high temperature gradient do not allow for complete crystallization or the formation of crystalline-type grains. Therefore, amorphous grains are formed in the liquidus-solidus regions at the liquid-solid transition. Short-term heating and high temperatures lead to an inhomogeneous structure. These thermal conditions do not allow for stationary diffusion to occur, and the individual components are largely retained in the stationary zones of the steel. As a result of the ferrite→austenite→ferrite phase transformations and the high ferrite transformation temperature (911°C), ferrite is preserved in the thermally affected SL, with low-carbon martensite (M) (C ↓) being registered in the partial transformation zones (Figure 11b). The relatively lower pearlite transformation temperature (727°C) and heating time favor the pearlite → austenite phase transformation in the pearlite colonies. In addition, the melting of pearlite occurs

more easily than that of ferrite; the temperature range between the solidus and liquidus is approximately 1320–1480 °C. As a result, a mixture of liquid and solid phases is obtained in the SLs, with the solid austenite phase undergoing a phase transformation to martensite. The high carbon content in the resulting martensite partially blocks further the austenite→martensite transition (M) (C↑)transformation because carbon is an austenite-retaining element, and thus a certain amount of austenite is retained (Figure 11b).

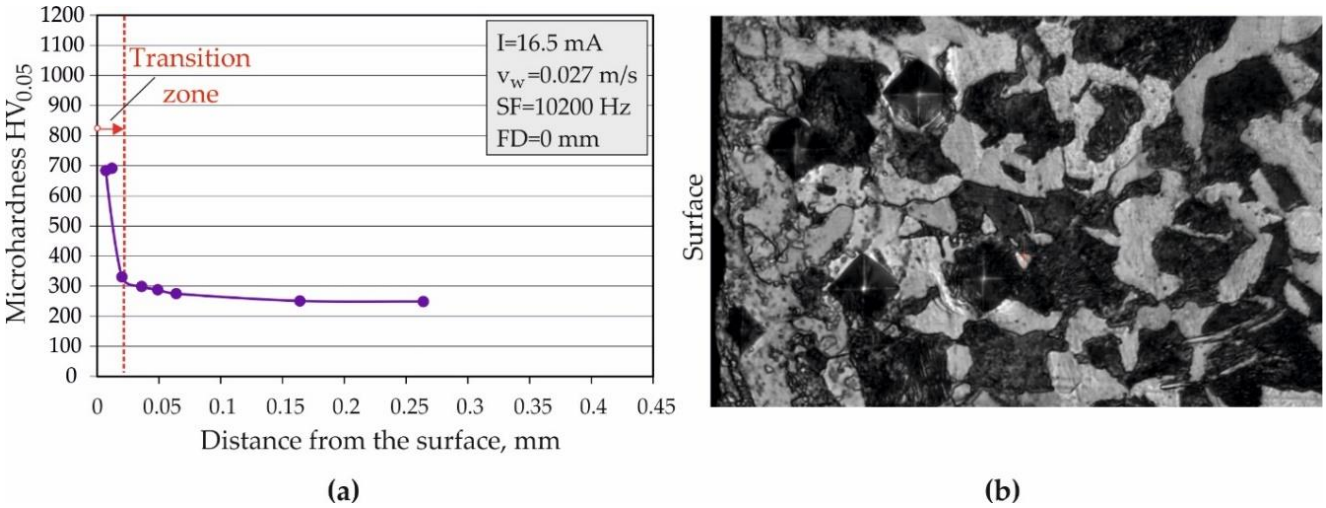

Figure 12.
Microhardness depth profile of the specimen treated with $I_b = 16.5$ mA.

The microhardness profile and optical image of the transition zone are shown in Figure 12a and 12b respectively. The microhardness profile (Figure 12a) confirms the transition zone depth shown in Figure 11a.

Increasing the electron beam current of $I_b = 30$ mA increases the transition zone depth (up to ~225 μm) (Figure 13). Three zones with characteristic phases and structural changes were formed. The particular combination of EBH process parameters facilitates the formation of fine-needle martensite in the upper SL (Figure 13b). In this layer, the temperature reached values characteristic of the zones above and between the liquidus and solidus lines of C45 steel. As a result of the high temperature gradient and the high cooling rate, amorphous grains form from the molten phase (Figure 13b). The high temperature partially influences the homogenization of the structure, in which hereditary ferrite is not observed. As a result, the carbon concentration in the martensite is reduced during the phase transformation.

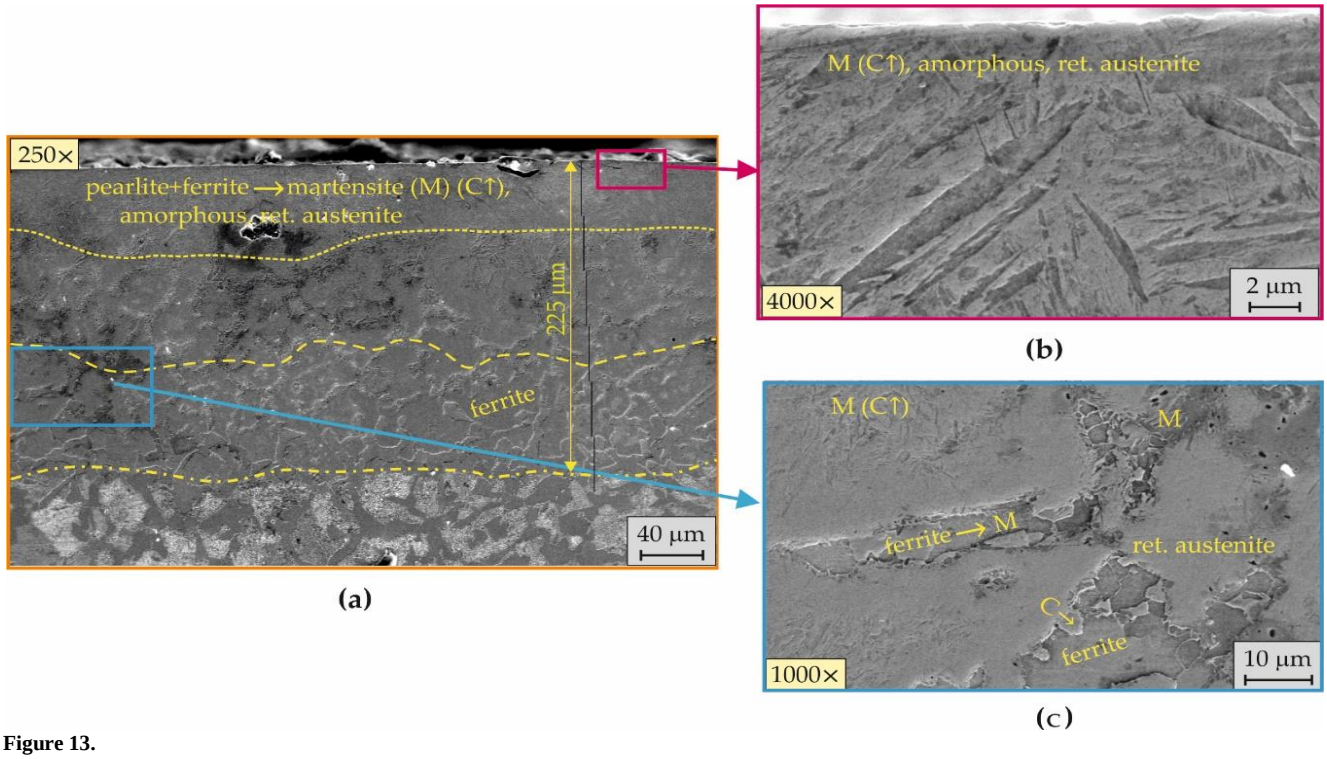

Figure 13.
Microstructure of the SLs after EBH with $I_b = 30$ mA.

Table 4 shows the percentage of retained austenite as a function of depth from the surface for the specimen treated with $I_b = 30$ mA. The phase analysis confirms the presence of retained austenite in the affected transition layer, with a variable trend in depth up to approximately 0.18 mm.

Table 4.
Percentage of retained austenite as a function of depth in the specimen treated with $I_b = 30$ mA

	Depth from the surface mm							
	0	**0.015**	**0.035**	**0.06**	**0.09**	**0.125**	**0.16**	**0.18**
Retained austenite, %	4.646	4.033	2.872	9.387	7.787	8.342	14.434	0

In the boundary region between the transition zone and the bulk material, the transformation of ferrite into martensite and zones with diffusion enrichment of the ferrite with carbon are observed (Figure 13c).

The microhardness depth profile of the specimen subjected to EBH with $I_b = 30$ mA is shown in Figure 14a. The highest measured microhardness occurs near the surface because of the resulting fine-needle martensite and the presence of a pseudo-amorphous structure in the upper SL. In the hardened transition zone, with a depth of approximately, 0.22 mm, the microhardness profile is characterized by notable peaks and dips (Figure 14a). Owing to the inhomogeneous structure, when the indenter enters a zone with hereditary ferrite, the microhardness decreases sharply (Figure 14b).

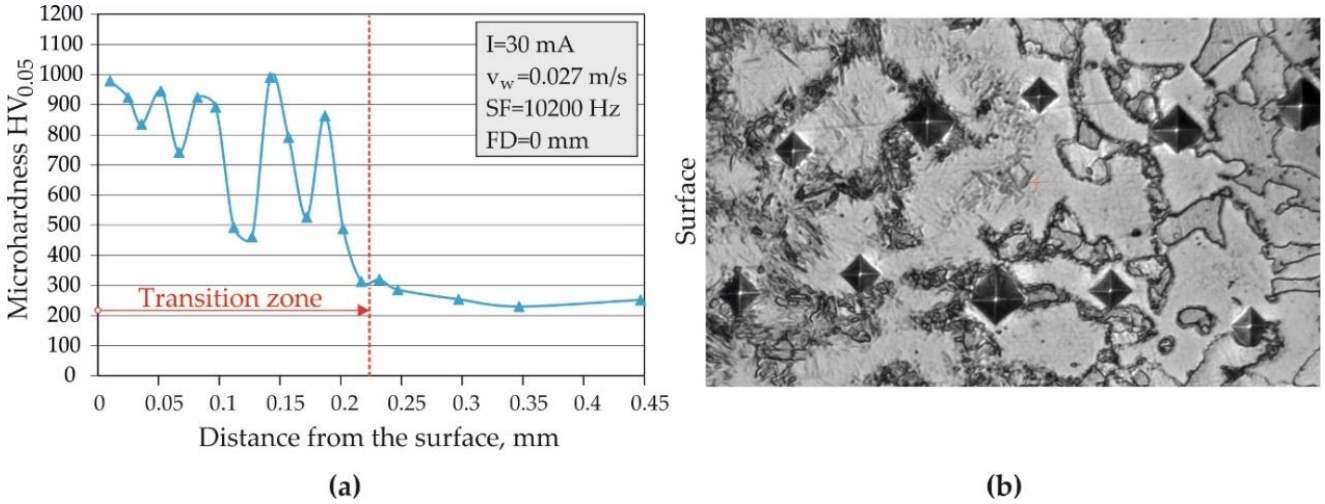

Figure 14.
Microhardness depth profile of the specimen treated with $I_b = 30$ mA.

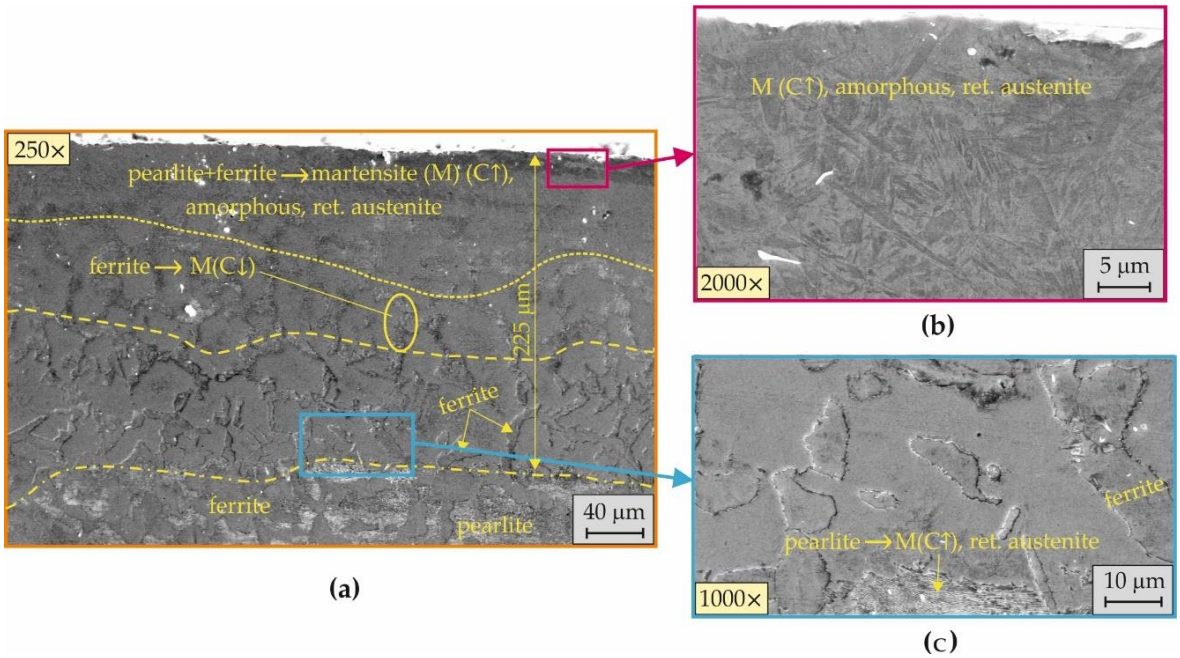

Figure 15.
Microstructure of the SLs after EBH with $I_b = 34.5$ mA.

Figure 15 shows the microstructure of the specimen treated with the largest investigated electron beam current, $I_b = 34.5$mA. The microstructural changes and the transition zone depth are similar to those observed in the specimen treated

with $I_b = 30mA$ (see Figure 13). In the upper SL, the two-phase structure transforms into needle-like martensite, amorphous grains, and retained austenite (Figure 15b). In the intermediate zone, a partial phase transformation of ferrite into low-carbon martensite is observed (Figure 15a). At the boundary with the bulk material, the pearlite colonies transform into martensite, amorphous grains, and retained austenite (Figure 15c).

The experimental results obtained for the microhardness depth profile of the specimen treated with $I_b = 34.5$ mA (Figure 16a,b) are similar to those obtained for the specimen treated with $I_b = 30$ mA. A key difference is the lower microhardness measured at the top SL (Figure 16a). This may be attributed to the presence of coarser martensite, formed under a higher power density.

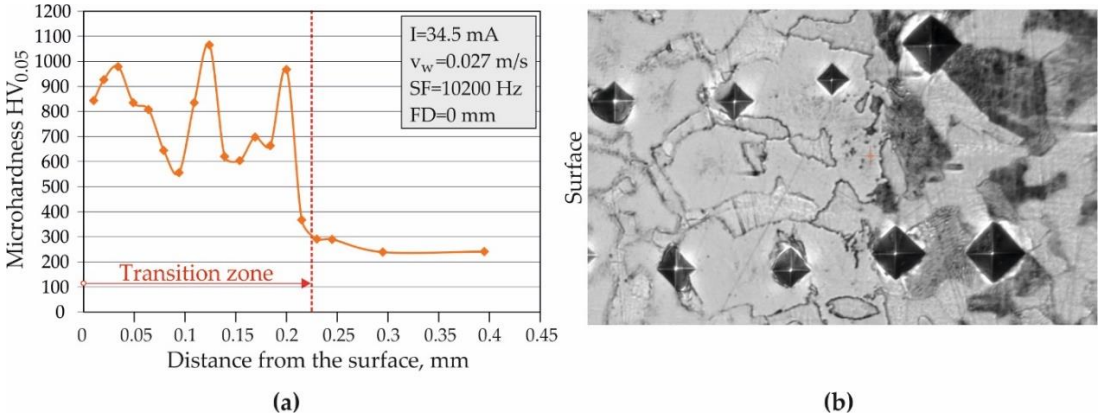

Figure 16.
Microhardness depth profile of the specimen treated with $I_b = 34.5$ mA.

The phases in the microstructures shown in Figures 11, 13, and 15 are confirmed by the phase analysis of the three specimens after EBH (Figure 17). In all three specimens, the presence of retained austenite was observed, as well as a broadening of the α–Fe peaks compared with those in the as-received state (see Figure 4). This broadening is an indicator of the resulting pseudo-amorphous structure in the upper SLs. Similarly, the amorphous state was observed in the SL of low-carbon steel (0.2 wt.% C), induced by high-current pulsed EBH [21].

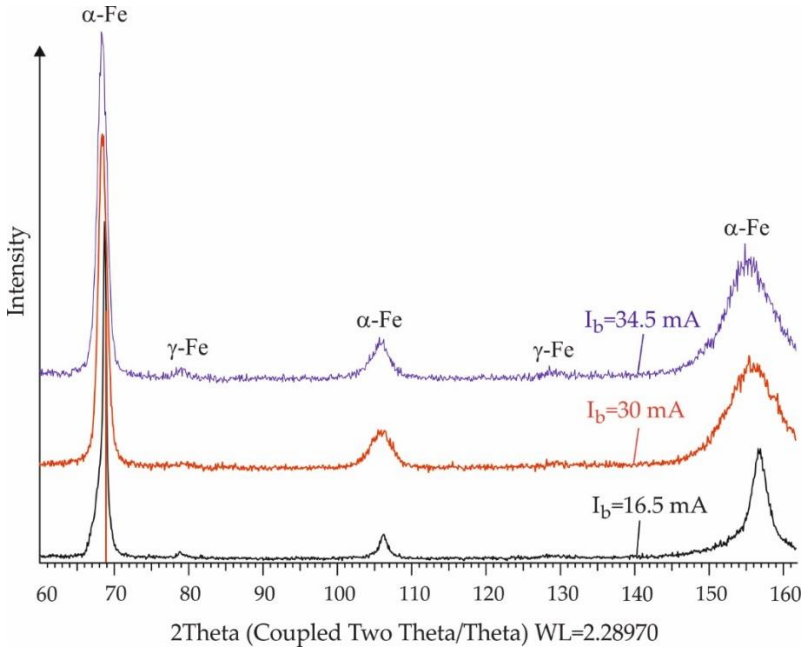

Figure 17.
Phase analysis of the three specimens prepared with different electron beam currents.

Kim and Thein [32] studied the LBH process of rod-shaped C45 (SM45C) steel specimens, emphasizing the surface hardening effect in correlation with the circumferential speed and theoretical overlap rate due to the helical motion of the laser beam relative to the processed cylindrical surface. They found that the longitudinal hardness distribution exhibited periodic increases and decreases with an approximate maximum value $HV_{0.2} = 780$. The novel EBH process discussed in the present study provides a 15.76% increase in the maximum surface microhardness of C45 steel (relative to the as-received condition) compared with that obtained in Kim and Thein [32]. Note that the linear scanning mode used in the EBH process provides several significant advantages compared with the conventional scanning mode [32]: 1) the overlapping effect in the axial direction and the associated periodic nature of the change in microhardness are eliminated,

and 2) a minimal overlapping effect is manifested in the circumferential direction without deteriorating the surface quality. The maximum surface microhardness ($HV_{0.05} = 903$) provided by the EBH process, the hardness is greater than the maximum value (approximately 830 VHN) measured in the central gauge section of rod-type AISI 4140 steel fatigue specimens after high-energy accelerated electron beam irradiation in air, using a spiral scan path [37].

5. Conclusions

This research introduces a novel EBH process for modifying as-received C45 steel cylindrical specimens, utilizing continuous irradiation with power levels ranging from P=720–2070 W and line scanning in the axial direction. The experimental study of the EBH process was performed using a one-factor-at-a-time approach, focusing on the influence of operating parameters on the resulting microhardness. The key findings are summarized as follows:

- The experimental results demonstrate the potential of the new EBH process for transformational surface hardening of C45 steel, providing superior microhardness. The obtained maximum microhardness of $HV_{0.05} = 903$ is three times higher than the microhardness obtained after turning.
- A distinctive feature of the novel EBH process is the linear scanning mode in the axial direction, which has two main effects: 1) it eliminates the overlapping effect typically observed in the axial direction and the associated periodic microhardness distribution, and 2) a minimal overlapping effect is manifested in the circumferential direction without degrading the surface quality.
- The electron beam current and workpiece velocity have the greatest impact on microhardness because they strongly affect the heat released in the SLs and the heating sand cooling rates.
- The SEM images confirmed the microstructural modification of the SLs due to martensitic transformation, and the transition layer depth strongly depends on the electron beam current. In addition, the created thermal conditions favor the formation of a pseudo-amorphous structure near the top SL. The presence of fine-needle martensite and pseudo-amorphous structure is the main factor maximizing the microhardness in the EBH process implemented with the following parameters: $I_b = 30$ mA, $v_w = 0.027$ m/s, SF = 10,200 Hz, and FL = 0 mm.
- Implementing the EBH process with opposite focal length values ($FL = \pm 5$ mm; $FL = \pm 10$ mm) results in practically the same surface microhardness and decreases the absolute value of the FL reduces the variation in the measured microhardness values.
- The following limitations were found regarding the suitable operating ranges: 1) the electron beam current of $I_b = 12$ mA is insufficient to affect the microhardness; 2) the scanning frequency of SF = 400 Hz leads to a relatively low microhardness, characterized by the greatest variation in the measured values, a noticeable overlapping effect in the circumferential direction, and markedly deteriorated roughness ($R_a = 5.74$ μm)3) the focal length values of $FL = \pm 15, \pm 20$ mm reduce the microhardness, significantly increasing the variation in the measured values. Therefore, these operating values fall outside the useful range and should be excluded. Therefore, suitable ranges of the operating parameter were determined herein (I_b of 16–30 mA, v_w of 0.022–0.036 m/s, SF of 5300–20,000 Hz, and FL of ±0–10 mm). These ranges are the basis for the experimental plan design of the novel EBH process.

Abbreviations:

EBH	Electron beam hardening
LBH	Laser beam hardening
SI	Surface integrity
SLs	Surface layers

List of symbols

A	Electron beam area
d	Electron beam diameter
FL	Focal length
HV_{init}	Initial microhardness
$HV_{0.05}$	Microhardness obtained after EBH
I_b	Electron beam current
P	Irradiation power
PD	Power density
R_a	Arithmetic average of the roughness profile after EBH
$R_{a,init}$	Arithmetic average of the roughness profile after turning
SF	Scanning frequency
v_w	Workpiece velocity

References

[1] J. T. Maximov, G. V. Duncheva, A. P. Anchev, and V. P. Dunchev, "Explicit correlation between surface integrity and fatigue limit of surface cold worked chromium-nickel austenitic stainless steels," *The International Journal of Advanced Manufacturing Technology*, vol. 133, no. 11, pp. 6041-6058, 2024. https://doi.org/10.1007/s00170-024-14113-6

[2] X. Han, Z. Zhang, B. Wang, S. J. Thrush, G. C. Barber, and F. Qiu, "Microstructures, compressive residual stress, friction behavior, and wear mechanism of quenched and tempered shot peened medium carbon steel," *Wear*, vol. 488-489, p. 204131, 2022. https://doi.org/10.1016/j.wear.2021.204131

[3] P. K. Dwivedi, A. K. Rai, P. Ganesh, K. Ranganathan, K. S. Bindra, and K. Dutta, "Effect of laser shock peening on microstructure and micro-texture evolution in high-strength low-alloy steel upon electrochemical interaction," *Journal of Materials Engineering and Performance*, vol. 33, no. 11, pp. 5206-5222, 2024. https://doi.org/10.1007/s11665-023-08356-9

[4] H. Soyama and A. M. Korsunsky, "A critical comparative review of cavitation peening and other surface peening methods," *Journal of Materials Processing Technology*, vol. 305, p. 117586, 2022. https://doi.org/10.1016/j.jmatprotec.2022.117586

[5] D. J. Noronha, S. Sharma, R. Prabhu Parkala, G. Shankar, N. Kumar, and S. Doddapaneni, "Deep rolling techniques: A comprehensive review of process parameters and impacts on the material properties of commercial steels," *Metals*, vol. 14, no. 6, p. 667, 2024. https://doi.org/10.3390/met14060667

[6] D. A. De Oliveira, A. M. Martins, A. J. D. Santos, F. de Castro MagalhŃes, and A. M. AbrŃo, "Influence of the hydrostatic ball burnishing on surface quality and ultra-microhardness," *Journal of the Brazilian Society of Mechanical Sciences and Engineering*, vol. 46, no. 2, p. 74, 2024.

[7] J. T. Maximov and G. V. Duncheva, "Finite element analysis and optimization of spherical motion burnishing of low-alloy steel," *Proceedings of the Institution of Mechanical Engineers, Part C: Journal of Mechanical Engineering Science*, vol. 226, no. 1, pp. 161-176, 2011. https://doi.org/10.1177/0954406211412024

[8] J. Maximov and G. Duncheva, "The correlation between surface integrity and operating behaviour of slide burnished components—a review and prospects," *Applied Sciences*, vol. 13, no. 5, p. 3313, 2023. https://doi.org/10.3390/app13053313

[9] J. Maximov, G. Duncheva, M. Ichkova, and K. Anastasov, "Optimal diamond burnishing of chromium–nickel austenitic stainless steels based on the finishing process–surface integrity–operating behavior correlations," *Metals*, vol. 15, no. 6, p. 574, 2025. https://doi.org/10.3390/met15060574

[10] Z. Stević *et al.*, "The design of a system for the induction hardening of steels using simulation parameters," *Applied Sciences*, vol. 13, no. 20, p. 11432, 2023. https://doi.org/10.3390/app132011432

[11] P. D. Babu and P. Marimuthu, "Status of laser transformation hardening of steel and its alloys: A review," *Emerging Materials Research*, vol. 8, no. 2, pp. 188-205, 2019. https://doi.org/10.1680/jemmr.16.00145

[12] S. Valkov, M. Ormanova, and P. Petrov, "Electron-beam surface treatment of metals and alloys: Techniques and trends," *Metals*, vol. 10, no. 9, p. 1219, 2020. https://doi.org/10.3390/met10091219

[13] J. Cai, P. Lv, C. L. Zhang, J. Wu, C. Li, and Q. F. Guan, "Microstructure and properties of low carbon steel after surface alloying induced by high current pulsed electron beam," *Nuclear Instruments and Methods in Physics Research Section B: Beam Interactions with Materials and Atoms*, vol. 410, pp. 47-52, 2017. https://doi.org/10.1016/j.nimb.2017.08.007

[14] O. Chudina and Y. Luzhnov, "The concept of structural steels surface hardening for tribo-joint elements," *IOP Conference Series: Materials Science and Engineering*, vol. 1159, p. 012080, 2021. https://doi.org/10.1088/1757-899X/1159/1/012080

[15] I. A. Bataev *et al.*, "Non-vacuum electron-beam carburizing and surface hardening of mild steel," *Applied Surface Science*, vol. 322, pp. 6-14, 2014. https://doi.org/10.1016/j.apsusc.2014.09.137

[16] I. A. Bataev *et al.*, "Structure and tribological properties of steel after non-vacuum electron beam cladding of Ti, Mo and graphite powders," *Materials Characterization*, vol. 112, pp. 60-67, 2016. https://doi.org/10.1016/j.matchar.2015.11.028

[17] P. Hollmann *et al.*, "Investigation of cracking prevention in magnetron-sputtered TiAlN coatings during subsequent electron beam hardening," *Surface and Coatings Technology*, vol. 338, pp. 75-83, 2018. https://doi.org/10.1016/j.surfcoat.2017.12.042

[18] T. S. Ogneva *et al.*, "Structure and oxidation behavior of nial-based coatings produced by non-vacuum electron beam cladding on low-carbon steel," *Metals*, vol. 12, no. 10, p. 1679, 2022. https://doi.org/10.3390/met12101679

[19] I. A. Bataev *et al.*, "Surface hardening of steels with carbon by non-vacuum electron-beam processing," *Surface and Coatings Technology*, vol. 242, pp. 164-169, 2014. https://doi.org/10.1016/j.surfcoat.2014.01.038

[20] Y. Fu, J. Hu, X. Zhang, W. Huo, X. Cao, and W. Zhao, "Surface modification of AISI 1045 steel by pseudospark based pulsed electron beam," *Nuclear Instruments and Methods in Physics Research Section B: Beam Interactions with Materials and Atoms*, vol. 434, pp. 88-92, 2018. https://doi.org/10.1016/j.nimb.2018.08.023

[21] Q. F. Guan *et al.*, "Surface nanostructure and amorphous state of a low carbon steel induced by high-current pulsed electron beam," *Surface and Coatings Technology*, vol. 196, no. 1, pp. 145-149, 2005. https://doi.org/10.1016/j.surfcoat.2004.08.104

[22] J. Matlák, R. Foret, and I. Dlouhý, "Properties of electron beam hardened layers made by different beam deflection," *Manufacturing Technology*, vol. 18, no. 2, pp. 279–284, 2018. https://doi.org/10.21062/ujep/91.2018/a/1213-2489/MT/18/2/279

[23] I. Maamri, N. Barka, and A. El Ouafi, "ANN laser hardening quality modeling using geometrical and punctual characterizing approaches," *Coatings*, vol. 8, no. 6, p. 226, 2018. https://doi.org/10.3390/coatings8060226

[24] X. Cao, J. Hu, W. Huo, X. Xi, and W. Zhao, "Surface microstructure and property modifications in AISI 304 stainless steel induced by pseudospark pulsed electron beam treatments," *Vacuum*, vol. 184, p. 109914, 2021. https://doi.org/10.1016/j.vacuum.2020.109914

[25] Z. Feng *et al.*, "Effect of high current pulsed electron beam on surface microstructure and properties of cold-rolled austenitic stainless steel," *Journal of Materials Research and Technology*, vol. 29, pp. 1183-1193, 2024. https://doi.org/10.1016/j.jmrt.2024.01.103

[26] S. Konovalov, Y. Ivanov, V. Gromov, and I. Panchenko, "Fatigue-induced evolution of AISI 310S steel microstructure after electron beam treatment," *Materials*, vol. 13, no. 20, p. 4567, 2020. https://doi.org/10.3390/ma13204567

[27] J. Lu *et al.*, "Rapid synthesis of ultra-wear-resistant nanocrystallite stainless steel via electron beam direct irradiation," *Surface and Coatings Technology*, vol. 483, p. 130714, 2024. https://doi.org/10.1016/j.surfcoat.2024.130714

[28] J. Jin, R. Gao, H. Peng, H. Guo, S. Gong, and B. Chen, "Rapid solidification microstructure and carbide precipitation behavior in electron beam melted high-speed steel," *Metallurgical and Materials Transactions A*, vol. 51, no. 5, pp. 2411-2429, 2020. https://doi.org/10.1007/s11661-020-05661-z

[29] E. Prokhorenko *et al.*, "Modification of structure of the surface of steel (ХГС) as a result of influences of high-current electron beam," *Problems of Atomic Science and Technology*, vol. 2, no. 126, pp. 47–53, 2020.

[30] S. Guarino, M. Barletta, and A. Afilal, "High power diode laser (HPDL) surface hardening of low carbon steel: Fatigue life improvement analysis," *Journal of Manufacturing Processes*, vol. 28, pp. 266-271, 2017.

[31] A. Fortunato, A. Ascari, E. Liverani, L. Orazi, and G. Cuccolini, "A comprehensive model for laser hardening of carbon steels," *Journal of Manufacturing Science and Engineering*, vol. 135, no. 6, p. 061002, 2013. https://doi.org/10.1115/MSEC2013-1094

[32] V. A. Kim and A. N. Thein, "Quantitative assessment of dissipative properties of superficial structure of the steel 25xm strengthened by pulse laser influence," *Solid State Phenomena*, vol. 299, pp. 933-937, 2020. https://doi.org/10.4028/www.scientific.net/SSP.299.933

[33] L. Orazi, A. Fortunato, G. Cuccolini, and G. Tani, "An efficient model for laser surface hardening of hypo-eutectoid steels," *Applied Surface Science*, vol. 256, no. 6, pp. 1913-1919, 2010. https://doi.org/10.1016/j.apsusc.2009.10.037

[34] S. Martínez, A. Lamikiz, E. Ukar, A. Calleja, J. Arrizubieta, and L. L. De Lacalle, "Analysis of the regimes in the scanner-based laser hardening process," *Optics and Lasers in Engineering*, vol. 90, pp. 72-80, 2017. http://dx.doi.org/10.1016/j.optlaseng.2016.10.005

[35] K. Jong-Do, L. Myeong-Hoon, L. Su-Jin, and K. Woon-Ju, "Laser transformation hardening on rod-shaped carbon steel by Gaussian beam," *Transactions of Nonferrous Metals Society of China*, vol. 19, no. 4, pp. 941-945, 2009.

[36] N. Maharjan, W. Zhou, Y. Zhou, Y. Guan, and N. Wu, "Comparative study of laser surface hardening of 50CrMo4 steel using continuous-wave laser and pulsed lasers with ms, ns, ps and fs pulse duration," *Surface and Coatings Technology*, vol. 366, pp. 311-320, 2019. https://doi.org/10.1016/j.surfcoat.2019.03.036

[37] S.-H. Choo, S. Lee, and M. G. Golkovski, "Effects of accelerated electron beam irradiation on surface hardening and fatigue properties in an AISI 4140 steel used for automotive crankshaft," *Materials Science and Engineering: A*, vol. 293, no. 1-2, pp. 56-70, 2000. https://doi.org/10.1016/S0921-5093(00)01207-7

[38] Y. Fu, J. Hu, X. Shen, Y. Wang, and W. Zhao, "Surface hardening of 30CrMnSiA steel using continuous electron beam," *Nuclear Instruments and Methods in Physics Research Section B: Beam Interactions with Materials and Atoms*, vol. 410, pp. 207-214, 2017. http://dx.doi.org/10.1016/j.nimb.2017.08.014

[39] P. Petrov, "Optimization of carbon steel electron-beam hardening," *Journal of Physics: Conference Series*, vol. 223, no. 1, p. 012029, 2010. https://doi.org/10.1088/1742-6596/223/1/012029

[40] D. Diffrac, *Quantitative analysis from calibration to reporting*. Germany: Bruker AXS GmbH: Karlsrue, 2018.